



City Research Online

City, University of London Institutional Repository

Citation: Wang, Z., Aouf, N., Pizarro, J. & Honvault, C. (2025). Robust Adversarial Attacks Detection for Deep Learning based Relative Pose Estimation for Space Rendezvous. *Advances in Space Research*, 75(1), pp. 560-575. doi: 10.1016/j.asr.2024.11.054

This is the accepted version of the paper.

This version of the publication may differ from the final published version.

Permanent repository link: <https://openaccess.city.ac.uk/id/eprint/34106/>

Link to published version: <https://doi.org/10.1016/j.asr.2024.11.054>

Copyright: City Research Online aims to make research outputs of City, University of London available to a wider audience. Copyright and Moral Rights remain with the author(s) and/or copyright holders. URLs from City Research Online may be freely distributed and linked to.

Reuse: Copies of full items can be used for personal research or study, educational, or not-for-profit purposes without prior permission or charge. Provided that the authors, title and full bibliographic details are credited, a hyperlink and/or URL is given for the original metadata page and the content is not changed in any way.

City Research Online:

<http://openaccess.city.ac.uk/>

publications@city.ac.uk

Robust Adversarial Attacks Detection for Deep Learning based Relative Pose Estimation for Space Rendezvous

Ziwei Wang^{a,1,*}, Nabil Aouf^{a,2}, Jose Pizarro^b, Christophe Honvault^b

^aDepartment of Engineering, City, University of London, Northampton Square, London, EC1V 0HB, United Kingdom

^bEuropean Space Research and Technology Centre, Keplerlaan 1, PO Box 299, Noordwijk, 2200 AG, The Netherlands

Abstract

Research on developing deep learning techniques for autonomous spacecraft relative navigation challenges is continuously growing in recent years. Adopting those techniques offers enhanced performance. However, such approaches also introduce heightened apprehensions regarding the trustability and security of such deep learning methods through their susceptibility to adversarial attacks. In this work, we propose a novel approach for adversarial attack detection for deep neural network-based relative pose estimation schemes based on the explainability concept. We develop for an orbital rendezvous scenario an innovative relative pose estimation technique adopting our proposed Convolutional Neural Network (CNN), which takes an image from the chaser's onboard camera and outputs accurately the target's relative position and rotation. We perturb seamlessly the input images using adversarial attacks that are generated by the Fast Gradient Sign Method (FGSM). The adversarial attack detector is then built based on a Long Short Term Memory (LSTM) network which takes the explainability measure namely SHapley Value from the CNN-based pose estimator and flags the detection of adversarial attacks when acting. Simulation results show that the proposed adversarial attack detector achieves a detection accuracy of 99.21%. Both the deep relative pose estimator and adversarial attack detector are then tested on real data captured from our laboratory-designed setup. The experimental results from our laboratory-designed setup demonstrate that the proposed adversarial attack detector achieves an average detection accuracy of 96.29%.

© 2024 COSPAR. Published by Elsevier Ltd All rights reserved.

Keywords: Pose Estimation; Deep Learning; Adversarial Attack ; Adversarial Attack Detection; Explainable Artificial Intelligence

1. Introduction

The growth of deep learning-based techniques has drawn increasing attention in various domains of application, such as image processing, speech recognition, and many other challenging Artificial Intelligence (AI) based tasks (Guo

et al., 2016). Vision-based autonomous orbital space rendezvous (Wie et al., 2014), is an application for which adopting deep learning approaches to spacecraft position and attitude estimation is continuously gaining interest within the research community and the space agencies (Song et al., 2022; Kisantal et al., 2020).

The state-of-the-art achievements in deep learning (DL) research demonstrate that the Convolutional Neural Networks (CNNs) have successfully gained outstanding performance in computer vision applications, such as object detection and target localisation (Ren et al., 2017; Redmon & Farhadi, 2018;

*Corresponding author

Email addresses: ziwei.wang.3@city.ac.uk (Ziwei Wang), nabil.aouf@city.ac.uk (Nabil Aouf), jose.pizarro@esa.int (Jose Pizarro), christophe.honvault@esa.int (Christophe Honvault)

¹Research Fellow, Department of Engineering

²Professor of Robotics and Autonomous Systems, Department of Engineering

Cebollada et al., 2022). Determining the pose of a spacecraft's relative state by processing input images is typically achieved through the six Degree-of-Freedom (6 DOF) pose estimation of the target object frame relative to the camera (onboard the spacecraft) frame. These vision-based pose estimation methods are traditionally computed by matching relative features on images captured by the camera to relative locations in the target frame. Different from the traditional approaches, the CNNs can be trained to detect features from raw image data and estimate the relative pose by regressing the position and attitude, without the need for manual feature engineering which is often required in traditional computer vision methods. The advantages of CNN-based pose estimation approaches are that they can potentially lead to better performance in complex orbital scenarios and more robustness to variations in lighting, viewpoint, and cluttered background.

Recent achievements in DL-based pose estimation demonstrate outstanding accuracy performance (Phisannupawong et al., 2020; Oestreich et al., 2020; Rondao et al., 2022; Chekakta et al., 2022). However, the vulnerability of such deep learning scheme can be questionable (Chawla et al., 2022; Nemcovsky et al., 2022; Tian et al., 2024). Indeed, minor changes in the spacecraft onboard camera acquired images that is used by the CNN-based pose estimator can cause CNNs to make wrong predictions due to their reliance on low-level affected features, such as edges and textures, and their high sensitivity to slight variations in the input space. Those changes in the input images and thus on features that the CNN-based pose estimation relies on can be caused by adversarial attacks (Lin et al., 2020). Adversarial attacks aim to make small perturbations to the input images that are imperceptible to human vision and can significantly affect the CNN's prediction (Grabinski et al., 2022). For real-world applications where CNNs are applied to estimate the relative pose of spacecraft, applying an adversarial attack to the input images can potentially make the CNNs output the wrong position or attitude of the target. This could seriously damage the autonomous rendezvous operation system if wrong pose data are involved to generate any further

actions, such as guidance commands for the spacecraft to rendezvous and/or dock to the target satellite.

One of the significant challenges associated with deep neural networks is that these models usually lack of transparency, which means people cannot understand how the deep neural networks achieve their decisions. To address this issue, explainable AI (XAI) aims to provide an understandable explanation for the AI models' decision-making process. By applying XAI methods to CNNs, such as Class Activation Mapping (CAM) (Pope et al., 2019), Layer-wise Relevance Propagation (LRP) (Nazari et al., 2022) and SHapley Additive exPlanation (SHAP) values (Lundberg & Lee, 2017), users can understand how CNNs work and why models output their relative pose predictions. This nice characteristic of XAI methods can potentially be adopted in detecting adversarial attacks on CNN models.

This work aims to present an innovative demonstration of the vulnerability of CNN-based spacecraft rendezvous relative pose estimation scheme to digital adversarial attacks on camera input images and proposes a novel method for detecting those adversarial attacks when they may occur. In this paper, a vision based orbital autonomous rendezvous dynamic scenario is simulated. A CNN-based pose estimator is designed and trained to estimate the relative position and attitude of the target satellite involving a modified Darknet-19 (Redmon & Farhadi, 2017) as a feature extractor. The Fast Gradient Sign Method (FGSM) is employed to introduce small perturbation attacks to the input images. Various configurations of the FGSM attack are developed to demonstrate the impact of digital adversarial attacks on the CNN-based pose estimator. An LSTM-based detector exploiting the explainable Shap values of the CNN based estimator is then proposed to detect the adversarial attacks acting on the input images and thus the CNN based estimator outputs. To this end, this paper makes the following contributions:

- Firstly, a CNN-based relative pose estimator for close-range rendezvous is introduced, which is subsequently formulated as the target DL-based navigation system against adversarial attacks.

- Secondly, the Fast Gradient Sign Method (FGSM) Goodfellow et al. (2014) is utilised to generate invisible perturbations in the input images, introducing a range of FGSM attack configurations to illustrate the effects of digital adversarial attacks on the CNN relative pose estimator.
- Then, an LSTM-based adversarial attacks detection mechanism is proposed, leveraging the explainable (SHAP) value (Lundberg & Lee, 2017) from the CNN-based navigation system to identify adversarial attacks affecting the input images.
- Subsequently, the CNN-based relative pose estimator and LSTM-based adversarial attacks detection mechanism have been evaluated in both synthetic data and real-world data obtained from our laboratory to demonstrate the performance of proposed frameworks.

The paper is organised as follows: Section 2 provides an overview of current DL-based spacecraft pose estimation approaches and discusses existing methods for detecting adversarial attacks. Section 3 outlines the proposed design of the CNN-based pose estimator, how to adopt FGSM attacks to the pose estimator, and the design of the LSTM-based adversarial attack detector. Section 4 presents the test experiments that are conducted on both simulation data and real-world data obtained from our laboratory. Finally, Section 5 concludes the paper and discusses future work.

2. Background and Related Works

2.1. DL-based Spacecraft Relative Pose Estimation

Sharma et al. (2018) proposed a relative pose classification network which is based on AlexNet (Krizhevsky et al., 2012) architecture for non-cooperative spacecraft. In their design, the convolutional layers in AlexNet are initially trained on ImageNet dataset (Deng et al., 2009) as feature extractors. The pre-trained feature extractors are adopted with two fully-connected layers and one classification layer with training on ten sets of synthetic images that were created from Tango spacecraft flown in the Prisma mission (Persson et al., 2006). Their work shows

that the CNN-based relative pose classification outperforms the accuracy of an architecture based on classical feature detection algorithms. However, this network is designed to output a coarse pose classification and cannot meet the precision requirements for fine position and attitude estimation missions.

Yang et al. (2021) have proposed a CNN-based pose estimation method to estimate the relative position and orientation of non-cooperative spacecraft. In their approach, the pre-trained ResNet-50 (He et al., 2016) is adopted as the feature extractor, and two fully-connected layers are concatenated after the feature extract to output the relative position and orientation of the target spacecraft, respectively. To adapt the network to estimate the relative pose of other similar spacecraft, an additional output layer is concatenated with the output of position and orientation to predict the category of the target spacecraft. Different from previous work introduced by Sharma et al. (2018), this work can output the relative position and orientation of the target spacecraft, instead of a coarse pose classification. Similarly, pre-trained ResNet has also been used as the backbone by Proença & Gao (2020). In this work, the estimation of position is achieved by two fully-connected layers with a simple regression, and the relative error is minimised based on the loss weight magnitudes. Then, the continuous attitude estimation is performed via classification with soft assignment coding (Liu et al., 2011).

Rather than estimating the relative pose of spacecraft by using a single input frame, consecutive image inputs have been considered by group previous work, named ChiNet (Rondao et al., 2022). The ChiNet featured a Recurrent Convolutional Neural Network (RCNN) architecture, which involves a modified Darknet-19 (Redmon & Farhadi, 2017) as an image feature extractor and followed by LSTM units to deal with the sequences of input images. The ChiNet takes 4-channels input which not only includes the RGB image but also a thermal image of the spacecraft that has been stacked to the fourth channel of input. The ChiNet also proposed a multistage optimisation approach to train the deep neural network to improve the performance in spacecraft relative pose estimation.

2.2. Explainability in CNNs

While recent approaches to DL-based spacecraft relative pose estimation demonstrate outstanding performance in terms of prediction accuracy, understanding how these models predict relative pose is essential for providing robust solutions for future space rendezvous missions. As a new approach solution, eXplainable AI (XAI) techniques offer the possibility to analyse gradients in DL models to indicate the significance of input variables in the estimation decision-making process.

Lundberg & Lee (2017) proposed the SHAP values to interpret complex machine learning models. The SHAP value is based on a concept from game theory called Shapley values. These are used to fairly distribute the payoff among the players of a cooperative game, where each player can have different skills and contributions. Similarly, SHAP values assign each feature an importance value for a particular prediction and provide insights into the contribution of each feature. By examining the SHAP values of machine learning models, we will be able to understand the predictions of complex machine learning models.

Contrastive gradient-based (CG) saliency maps (Simonyan et al., 2013) are visual explanation methods for deep neural networks. They produce a heat map where the norm of the model's gradients indicates the significance of input variables. The heat map highlights the areas in the input image that would change the output class if they were changed. By accessing the heat map, users can identify the most relevant features for the model's prediction.

Class Activation Mapping (CAM) (Zhou et al., 2016) generates visual explanation maps by finding the spatial locations in the input image that contribute the most to a specific prediction. The CAM is particularly helpful in image classification tasks through CNNs. Similarly, gradient-weighted CAM (Grad-CAM) (Selvaraju et al., 2017) extends the work of CAM and provides visual explanations for decisions made by a wide range of CNN-based methods. Grad-CAM utilises the gradients of any target concept, flowing into the final convolutional layer to produce a localisation map that highlights the important re-

gions in the input image for predicting the concept. These XAI methods interpret the CNNs, making people understand how and why CNNs make certain predictions. However, since then, there has been no specific analysis on interpreting the DL-based spacecraft relative pose estimation to improve their explainability.

2.3. Adversarial Attacks

Adversarial attacks for CNNs aim to make small perturbations on the original input images where original and perturbed images look similar in human vision but can significantly impact the CNNs' predictions. However, very limited research works are investigating how adversarial attacks can impact DL-based pose estimation systems. Chawla et al. (2022) demonstrate the effect of different types of adversarial attacks on the predictions of the DL-based pose estimation system. Their work shows that adversarial attacks can significantly impact monocular pose estimation networks, leading to increased trajectory drift and altered geometry. Similarly, Nemcovsky et al. (2022) illustrate that the physical passive path adversarial attacks can seriously increase the error margin of a visual odometry model which is used in autonomous navigation systems leading onto potential collisions.

The impacts of adversarial attacks have garnered significant attention in the DL-based autonomous systems. Ilahi et al. (2021) provide an extensive overview of recent methodologies for adversarial attacks on Deep Reinforcement Learning models applied to autonomous systems, as well as the existing techniques for mitigating these attacks. Wang & Aouf (2024) examine the effects of perceptual perturbations on vision-based autonomous driving systems and propose an optimised policy to counter adversarial attacks on observation perturbations. Tian et al. (2024) explore multi-label adversarial example attacks targeting multi-label False Data Injection Attacks for locational detectors, highlighting significant security vulnerabilities in DL-based smart grid systems.

To protect the DL-based system from adversarial attacks, Liu et al. (2020) proposed a detection method based on the robustness of the classification results. Their results show that

the detector performs well against gradient-based adversarial attacks. Our group work, Hickling et al. (2023) proposed a CNN-based adversarial attack detector and an LSTM-based adversarial attack detector for Deep Reinforcement Learning (DRL) based Uncrewed Aerial Vehicle guidance. The simulation results show that the LSTM-based adversarial attack detector leads to 90% detection accuracy on the DRL model. It also suggests that the LSTM-based detector performs much more accurately and quicker than the CNN-based adversarial attack detector. Indeed, the LSTM-based detector is demonstrated to meet the real-time requirement in DRL based guidance.

To the best of our knowledge, as of yet, there is no literature looking at the impact of adversarial attacks in spacecraft relative pose estimation and how to detect those adversarial attacks in DL-based spacecraft relative pose estimation systems and this work first time proposes this. Our objective is to ultimately create an adversarial attack detector for the space navigation system, which employs SHAP values explainability mechanism to detect and flag potential adversarial attacks.

3. Methodology

In this section, a CNN-based spacecraft relative pose estimator is newly designed with the aim of providing a reliable estimated position and attitude of the target spacecraft in as rendezvous scenario. Then, the FGSM attacks are adopted on the spacecraft onboard camera resulting in an adversarial image to evaluate the impacts on the proposed deep pose estimator. Next, SHAP values are introduced to generate XAI signatures for both adversarial and normal input images. Finally, an LSTM-based adversarial detector is proposed and trained, which learns normal and adversarial SHAP values to detect the adversarial attacks on the spacecraft relative pose estimator.

3.1. CNN-based Spacecraft Relative Pose estimator

3.1.1. Overall architecture design

Similar to most DL-based spacecraft relative pose estimation algorithms, CNN is applied to extract features in the proposed pose estimator. The overall design of the pose estimator follows the design methodology in ChiNet (Rondao et al., 2022). The

Darknet-19 (Redmon & Farhadi, 2017) is originally trained in ImageNet (Deng et al., 2009) dataset which has an input size of $244 \times 244 \times 3$. In our design, input images of the pose estimator have a larger size than ImageNet images. Therefore, the first convolutional layer in Darknet-19 is configured with a kernel size of 7×7 . Following the approach of Darknet-53 (Redmon & Farhadi, 2018), the maxpooling layers in the Darknet-19 are replaced by 3×3 convolution operation with a stride of 2. Similarly, as the Darknet-53 approaches, the residual connections are also adopted to the proposed pose estimator. Batch Normalisation (Ioffe & Szegedy, 2015) layers are applied after each convolutional layer.

Our deep spacecraft relative pose estimator aims to output the relative position and attitude of the target directly. Therefore, two separate FC layers are applied. The first FC layer involves 3 output nodes to output the relative position in (x, y, z) and the second FC layer adopts a 6-dimensional (6-D) vector to represent the relative attitude of the target spacecraft. Finally, two FC layers are concatenated together to output the relative 6-DOF pose. In the second FC layer, 6-D vectors are applied to represent the relative attitude of the target spacecraft, instead of using quaternion representation. The reason is that the relative pose estimator is designed as a regression problem where the output has to be continuous. However, the normal attitude representation of quaternion is discontinuous, due to its antipodal ambiguity, i.e. $-q = q$. Therefore, the proposed pose estimator applies the 6-D vector formulated by Zhou et al. (2019), which mapped the 3-dimensional rotations into a 6-D continuous rotation. The overall design of the spacecraft relative pose estimator is presented in Fig. 1.

3.1.2. Synthetic data generation

To train and test the spacecraft relative pose estimator, synthetic datasets are generated in Blender, which is an open-source 3D modelling software. The spacecraft target model used in the synthetic dataset generation is the Jason-1 satellite, which was downloaded from the NASA 3D Resources website (Jason-1 3D Model). Dynamic simulation of the rendezvous is developed to generate the synthetic dataset in which

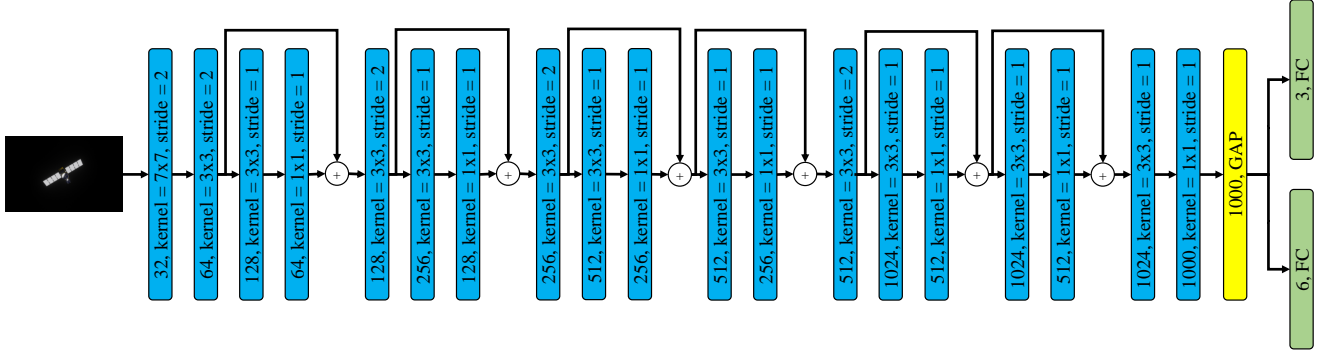


Fig. 1. The overall architecture of the proposed spacecraft relative pose estimator. The blue blocks represent the convolutional layers, which are formatted as (layer size, kernel size, stride). Each convolutional layer is followed by a batch normalisation layer and LeakyReLU activation. The yellow block indicates the Global Average Pooling (GAP) layer that downsamples the exacted features to a fixed 1D vector of 1000 units. The green blocks represent FC layers that will output the estimated relative position and attitude, respectively.

318 the camera onboard the chaser spacecraft starts at 60 metres
 319 away in z - axis from the target and end at 10 metres away
 320 from the target in z - axis, i.e. (0,0,10). Random rotation of
 321 the camera and target is considered in the synthetic data gen-
 322 eration. Many trajectory sequences are generated and each se-
 323 quence contains 2,500 RGB images. Each image has a size
 324 of 744×480 . To prevent overfitting in the deep relative pose
 325 estimator network, random rotation of the target spacecraft is
 326 applied to the model, and the camera is initialised at various
 327 positions in the synthetic data generation. Table 1 illustrates
 328 the synthetic dataset generated for training and validating the
 329 deep pose estimator.

Table 1. Example of synthetic data generated from Blender

Sequence ID	Start Position	Target Rotation
0	(0,0,60)	0
1	(-15,-25,60)	0
2	(-15,25,60)	0
3	(15,25,60)	0
4	(15,-25,60)	0
5	(-15,-10,60)	± 10 deg
6	(-15,10,60)	± 10 deg
7	(15,10,60)	± 10 deg
8	(15,-10,60)	± 10 deg
9	(-15,-10,60)	± 10 deg
10	(-15,10,60)	± 10 deg
11	(15,10,60)	± 10 deg
12	(15,-10,60)	± 10 deg

3.1.3. Loss Function

330 Training the spacecraft relative pose estimator can be for-
 331 mulated as a regression problem, where the total loss function
 332 combines the loss in position and loss in attitude. These are
 333 computed by Eq. (1) and Eq. (2), respectively, which were origi-
 334 nally proposed by Kendall et al. (2018). Followed by Rondao
 335 et al. (2022), a trainable weight is attributed to each loss, which
 336 corresponds to the task-specific variance of the Gaussian distri-
 337 bution. The total loss is then formulated in Eq. (3).
 338

$$L_p = \sum_{i=0}^B (\|p_{pred}^i - p_{gt}^i\|) \quad (1)$$

$$L_r = \sum_{i=0}^B (\|r_{pred}^i - r_{gt}^i\|) \quad (2)$$

$$L_{total} = \exp(-2\sigma_p)L_p + \exp(-2\sigma_r)L_r + 2(\sigma_p + \sigma_r) \quad (3)$$

339 where the p_{pred} and r_{pred} indicate the predicted position and
 340 attitude, and p_{gt} and r_{gt} indicate the ground truths position and
 341 attitude, respectively. B is the batch size and $\|\cdot\|$ donates the L_2
 342 norm. σ_p and σ_r represent the learnable weights for position
 343 and attitude, respectively.

3.2. Adversarial Attacks

344 In this work, the adversarial examples are generated by
 345 FGSM attacks (Goodfellow et al., 2014). The FGSM attacks
 346 aim to add small perturbations to the input images which will
 347

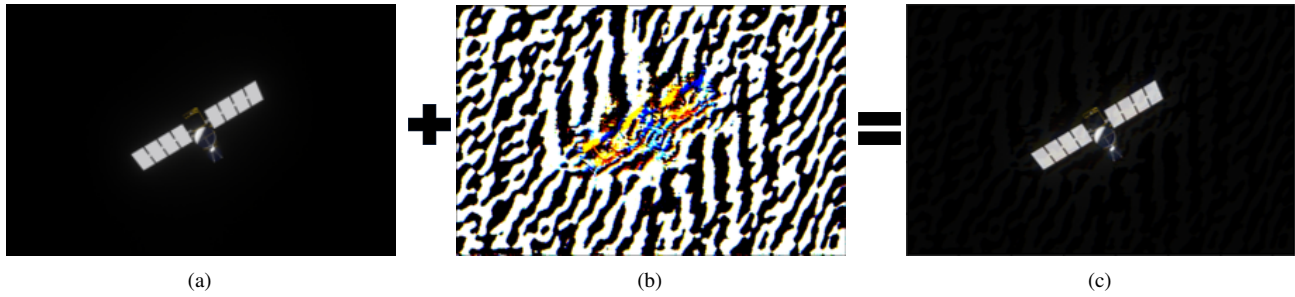


Fig. 2. An example of applying FGSM attacks to the input image. (a) the original input image. (b) perturbation patch with $\epsilon = 0.05$. (c) resultant adversarial image.

348 maximise the network's loss. The efficacy of adversarial at-
 349 tacks, including the FGSM attacks used in this work, can be
 350 influenced by the backbone neural network employed in per-
 351 ception systems. Different neural network architectures may
 352 exhibit varying levels of robustness and vulnerability to spe-
 353 cific types of adversarial attacks. Therefore, the effectiveness
 354 of these adversarial patches is inherently related to the specific
 355 CNN architectures employed. The equation in Eq. (4) describes
 356 how to generate an adversarial example for a given input image
 357 x by FGSM attack.

$$x' = x + \epsilon \times \text{sign}(\nabla_x L(\theta, x, y)) \quad (4)$$

358 where ϵ is a value of the perturbation effect which describes
 359 how strong the attack is. L is the loss of the input x with ground
 360 truth of y . The ∇_x calculates the loss gradient, L for input im-
 361 age x with relative ground truth y , and θ indicates the trained
 362 network's parameters. Depending on the quality of input im-
 363 ages and the attack strength, the result of the FGSM attack can
 364 be modified by changing the ϵ value.

365 In real implementation, the ϵ needs to be small enough to
 366 ensure the perturbations on the input image are seamless and
 367 cannot be visible by human vision but still significantly change
 368 the deep model's predictions. The ϵ value should be in the range
 369 of $(0,1)$, where a value of 0 means the adversarial image will
 370 be the same as the input image without any perturbation and
 371 a value of 1 means the adversarial image will be perturbed as
 372 significant distorted image to human vision. Fig. 2 illustrates
 373 an example of applying FGSM attacks to input images of the
 374 spacecraft relative deep pose estimator.

3.3. Explanability and Adversarial Attacks Detector 375

3.3.1. Explanability via DeepSHAP 376

377 The black-box nature of deep neural networks makes users
 378 can only observe the prediction of these models, but do not
 379 know the reasons for getting correct or wrong predictions. XAI
 380 techniques are developed to interpret the DL models. When the
 381 model's prediction is changed, the XAI will generate relative
 382 explanations to explain why the model is getting the prediction.
 383 In this work, we proposed a novel approach that adopts XAI
 384 techniques by applying the change in SHAP values of the input
 385 images as a measure to determine whether an adversarial attack
 386 happens on input images.

387 Originally, SHAP is proposed based on the idea of Shap-
 388 ley values, which are designed to assign a credit to every in-
 389 put feature for a given prediction. Generating SHAP values
 390 for DNNs can be computationally expensive, as the DNNs nor-
 391 mally contain a huge amount of features. Thanks to the work of
 392 DeepLIFT (Shrikumar et al., 2017), Shapley values for DNNs
 393 can be estimated by linearising the non-linear components of a
 394 neural network, a method referred to as DeepSHAP (Lundberg
 395 & Lee, 2017). This is achieved by utilising a reference input
 396 distribution, which can be linearly approximated, to estimate
 397 the expected value for the entire model.

398 However, directly generating SHAP values for the spacecraft
 399 relative pose estimator still requires a large amount of computa-
 400 tional resources. The pose estimator is based on CNNs with im-
 401 age inputs that contain thousands of pixels. Using DeepSHAP
 402 for image input requires generating Shapley values for each sin-
 403 gle pixel for every output neuron. Therefore, in this work, we

404 consider computing the SHAP values for the subsampling layer
 405 in the pose estimator, instead of computing them for the input
 406 image. As demonstrated previously, the spacecraft relative pose
 407 estimator contains a GAP layer that downsamples feature maps
 408 from the prior convolutional layer to 1000 samples. For exam-
 409 ple, computing SHAP values for a 744×480 RGB image needs
 410 to compute 1,071,360 pixels, instead, the GAP layer in the pose
 411 estimator only employs 1000 neurons. As a result, SHAP val-
 412 ues are generated for the outputs of the GAP layer that only
 413 need to compute 1000 features. This saving in the computation
 414 makes the generation of SHAP values for the deep pose estima-
 415 tor could potentially meet the implementation time constraints.

416 3.3.2. Adversarial attack detector

417 To detect any incoming adversarial attacks on the spacecraft
 418 deep relative pose estimator through the onboard camera, an
 419 LSTM-based adversarial attacks detector is proposed. The de-
 420 tector aims to monitor the SHAP values generated from the out-
 421 put of the GAP layer and detect any slight anomaly changes that
 422 could result based an adversarial attack. The LSTM is a type
 423 of Recurrent Neural Networks (RNNs) that is widely used in
 424 learning from time-series data, such as speech recognition (Yu
 425 et al., 2019). The LSTM architecture was originally proposed to
 426 address the long-term dependency issue in conventional RNNs.
 427 It can enable the propagation and representation of information
 428 over a sequence without causing useful information from dis-
 429 tant past time steps to be ignored.

430 In our approach, the SHAP values are generated based on
 431 the prediction of each output neuron in the proposed deep pose
 432 estimator. Different from applying adversarial attacks on a clas-
 433 sification CNN that only change the output label, when an at-
 434 tack occurs on the deep pose estimator, it could affect all output
 435 neurons to estimate for wrong position and attitude. Therefore,
 436 it can be assumed that there might exist a certain level of depen-
 437 dencies among those output neurons. From this point of view,
 438 building an LSTM-based adversarial attack detector can poten-
 439 tially achieve high detection accuracy.

440 Fig. 3 introduces the architecture of the proposed adversar-
 441 ial attack detector. The detector takes the SHAP values that are

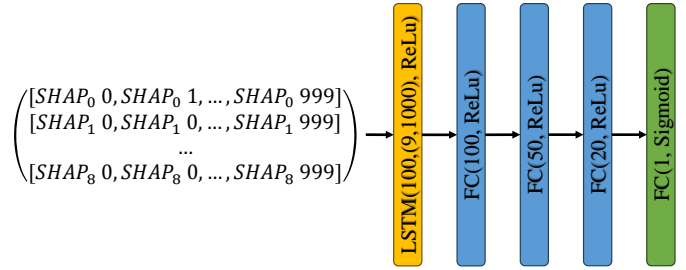


Fig. 3. Proposed adversarial attack detector. The yellow block indicates the LSTM layer which has an input shape of (9,1000) and an output space of 100. ReLu is applied as the activation function for the LSTM layer. The blue blocks are FC layers in the format of (units, activation). The green block indicates the output layer of the adversarial detector, which is also formed from the FC layer and outputs a Boolean to detect adversarial attacks.

442 computed from the GAP layer of the deep pose estimator. As
 443 there are nine output neurons in the proposed deep pose estima-
 444 tor, the shape of the SHAP values is (9, 1000). To input SHAP
 445 values to the detector, the SHAP values are formatted as a se-
 446 quence data with a length of 9. The detector outputs a Boolean,
 447 *True/False*, to indicate the result of detecting adversarial at-
 448 tacks.

449 4. Experimental Results

450 To validate our adversarial detection approach, two experi-
 451 ments are performed. The first experiment is built on the simu-
 452 lation environment with synthetic data as mentioned in Sec-
 453 tion 3. The second experiment is built on our lab environment
 454 to testing our approach with real data. For both sets of experi-
 455 ments, the spacecraft deep relative pose estimator and the ad-
 456 versarial attack detector are tested for their relevant accuracy,
 457 and then the two systems are integrated to test the overall suc-
 458 cessful detection rate of adversarial attacks.

459 4.1. Results on Synthetic Data

460 4.1.1. Accuracy of the Spacecraft Deep Relative Pose Estima-
 461 tor

462 To train the deep relative pose estimator, image data are col-
 463 lected from the Blender 3D model. There are 13 sequences of
 464 images generated from Blender with the relevant trajectories
 465 that are mentioned in Table 1. By following the trajectories in

466 Table 1, 2,500 images are generated for each trajectory, result-
 467 ing in a dataset with 32,500 images for training and testing in
 468 total. Fig. 4 shows two examples of synthetic data generation
 469 in Blender.

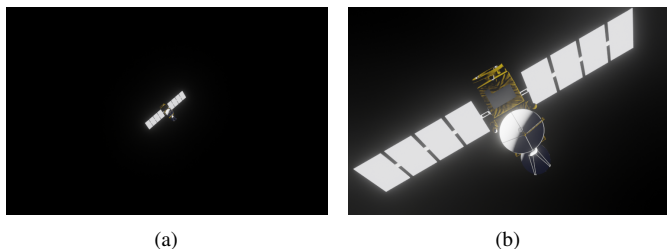


Fig. 4. Examples of synthetic data generated from Blender. (a) image captured at a camera position of (0, 0, 60m). (b) image captured at a camera position of (0, 0, 10m). Random rotation is applied to the target spacecraft.

470 The synthetic dataset is split by a train-test ratio of 0.8, i.e.
 471 80% of images in the dataset are used for training the deep re-
 472 lative pose estimator, and 20% of images are used to test the
 473 model's accuracy. Each image is associated with a ground truth
 474 label in the format of $(x, y, z, w, x_i, y_j, z_k)$. The first three ele-
 475 ments in the ground truth label represent the relative position of
 476 the chaser onboard camera to the target and the rest 4 elements
 477 represent the target attitude in quaternion representations in the
 478 chaser camera frame. The deep relative pose estimator outputs
 479 the attitude in a 6-D vector. Therefore, to calculate the loss
 480 in attitude, the quaternion representations are converted to the
 481 6-D vector representation by following the approach in (Zhou
 482 et al., 2019). A dropout rate of 0.2 is applied to the GAP layer in
 483 the training process. Multiple data augmentation techniques are
 484 considered in training the deep relative pose estimator, includ-
 485 ing Gaussian blur, Gaussian noise, image compression, random
 486 brightness and so on. These techniques help to prevent the
 487 model from overfitting the training dataset. The deep relative
 488 pose estimator is trained by stochastic gradient descent with an
 489 Adam optimiser. The triangular2 (Smith, 2017) policy is ap-
 490 plied for cycling learning rate with base learning of $2.5e-5$.

491 After training the deep relative pose estimator for 50 epochs
 492 with the training batch size of 32, The model's average predic-
 493 tion accuracy for both training and test datasets is reported in
 494 Fig. 5. In this experiment, the position error is measured by

Eq. (5) and the attitude error is measured by Eq. (6). 495

$$p_{err} := \|p_{pred} - p_{gt}\| \quad (5) \quad 496$$

$$r_{err} := 2 \arccos(q_{pred}^{-1} \otimes q_{gt}) \quad (6) \quad 497$$

where p_{pred} and p_{gt} represent the prediction of position and the
 497 ground truth of position magnitude. The q_{pred} and q_{gt} indicate
 498 the prediction of attitude and the ground truth of attitude in
 499 quaternion representation. The \otimes denotes the quaternion multi-
 500 plication and $\|\cdot\|$ denotes the L_2 norm. 501



Fig. 5. The prediction accuracy of the proposed pose estimator on training and test dataset after 50 epochs. The blue bar presents the average error on training data and the orange bar represents the average error on test data

502 The proposed spacecraft relative pose estimator achieves an
 503 accuracy of around 0.49m in position error and 0.68 deg in atti-
 504 tude error on the test dataset. Table 2 reports a comparison
 505 between the proposed deep relative pose estimator and state-
 506 of-the-art performance of other DL-based space relative pose
 507 estimation approaches based on their datasets. The comparison
 508 here aims to show that the proposed spacecraft deep relative
 509 pose estimator can achieve relatively good performance on the
 510 synthetic data and can be applied as a baseline model to imple-
 511 ment the adversarial attack algorithm on and test the adversarial
 512 attack detector. The comparison is not meant to be a quantita-
 513 tive benchmark evaluation of our approach relative to existing
 514 performing approaches.

4.1.2. FGSM Adversarial Attacks 515

As discussed in Section 3, the perturbation made by FGSM 516
 attacks can be adjusted by changing the ϵ value. To investi- 517

Table 2. Comparison with other approaches in DL-based space relative pose estimation

Model	Dataset	Position Error (m)	Attitude Error (deg)
Pronça & Gao (2020)	SPEED (Kelvins - ESA's Advanced Concepts Competition Website)	0.56	8.0
Rondao et al. (2022)	Synthetic	1.73	6.62
Yang et al. (2021)	Synthetic	[0.052, 0.039, 0.077]	[0.213, 0.233, 0.097]
Ours	Synthetic	0.49	0.68

518 gate the impact of adversarial attacks on DL-based space rela-
 519 tive pose estimation, different ϵ values are selected to generate
 520 adversarial onboard camera image input to the proposed deep
 521 relative pose estimator. Typically, the ϵ applied in this experi-
 522 ment are 1, 0.5, 0.3, 0.1, 0.05 and 0.01. The larger value of ϵ is,
 523 the more perturbations are made to images. The FGSM attack
 524 is applied to all synthetic test data, where all images in the test
 525 data. Then, the perturbed images are fed to the deep relative
 526 pose estimator for testing the impact of the FGSM attack. The
 527 average prediction relative pose errors of applying different ϵ
 values are reported in Fig. 6.

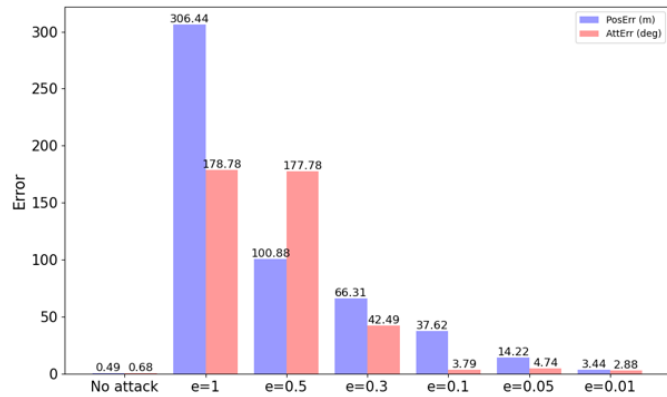


Fig. 6. Comparison of the prediction error of pose estimator under FGSM attack on test data with various ϵ values. The blue bar indicates the average position error and the red bar indicates the average attitude error on test data. The error magnitude for the position is metres and the error magnitude in rotation is measured by degrees.

528 We can see that as the ϵ value increases, the deep model's
 529 prediction error becomes larger. The attitude error is quite stable
 530 on $\epsilon = 0.1, 0.05$ and 0.01 , but has a dramatic increase if the
 531 $\epsilon > 0.3$.

532 To assess well how the adversarial attack can impact the
 533 DL-based navigation system in a space rendezvous scenario,
 534 a simple guidance scheme is implemented with the proposed
 535 deep relative pose estimator. The guidance scheme takes the
 536

537 estimated relative pose from the proposed deep relative pose
 538 estimator and then provides relative control actions to move
 539 the camera (spacecraft) to the target position. In the guidance
 540 scheme, the camera has an initial position of $(0, 0, 60)$ and a
 541 target position of $(0, 0, 10)$ with $\pm 1m$ tolerance. The guidance
 542 scheme updates the camera position with a maximum velocity
 543 of $1m/s$, as described in Eq. (7) and Eq. (8)

$$p_{new} = \begin{cases} p_{est} - 1 & \text{if } diff \geq 1 \\ p_{est} - diff & \text{otherwise} \end{cases} \quad (7)$$

$$diff = p_{est} - p_{tar} \quad (8)$$

545 where p_{new} , p_{est} , p_{tar} present the updated position, estimated
 546 position and target position of the camera, respectively. The
 test system is implemented as shown in Fig. 7.

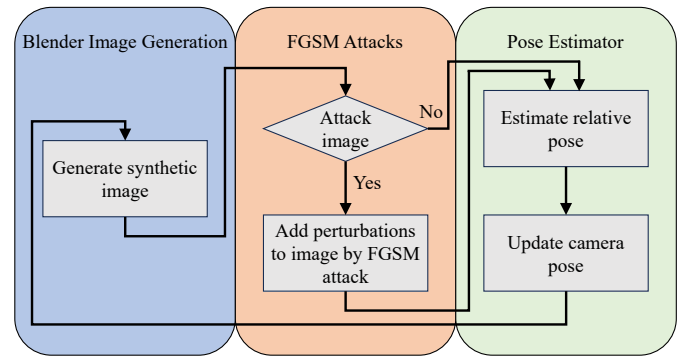


Fig. 7. Test system for proposed pose estimator on Blender in simulated space rendezvous scenario.

547 In this experiment, the test system is continuously attacked
 548 by FGSM on image data with various acquired camera frames.
 549 The *success* attack is defined as the camera (spacecraft) missing
 550 the target position while the *failure* attack means that the cam-
 551 era (spacecraft) can still reach the target position under continu-
 552 ous FGSM attack. Experimental results are reported in Table 3
 553 - 7.
 554

Table 3. FGSM attacks on the simulated space rendezvous scenario with $\epsilon=0.5$
 $\epsilon = 0.5$

Continuously Attacked Frame	5	10	15	20	
Attack start point (m)	60	failure	failure	failure	Success
	50	failure	failure	failure	Success
	40	failure	failure	Success	Success
	30	failure	failure	Success	Success
	20	failure	Success	Success	Success
	10	Success	Success	Success	Success

Table 4. FGSM attacks on the simulated space rendezvous scenario with $\epsilon=0.3$
 $\epsilon = 0.3$

Continuously Attacked Frame	5	10	15	20	
Attack start point (m)	60	failure	failure	failure	Success
	50	failure	failure	Success	Success
	40	failure	failure	Success	Success
	30	failure	failure	Success	Success
	20	failure	Success	Success	Success
	10	failure	Success	Success	Success

Table 5. FGSM attacks on the simulated space rendezvous scenario with $\epsilon=0.1$
 $\epsilon = 0.1$

Continuously Attacked Frame	5	10	15	20	
Attack start point (m)	60	failure	failure	failure	failure
	50	failure	failure	failure	failure
	40	failure	failure	failure	Success
	30	failure	failure	failure	failure
	20	failure	failure	failure	failure
	10	failure	failure	failure	Success

Table 6. FGSM attacks on the simulated space rendezvous scenario with $\epsilon=0.05$
 $\epsilon = 0.05$

Continuously Attacked Frame	5	10	15	20	
Attack start point (m)	60	failure	failure	failure	failure
	50	failure	failure	failure	Success
	40	failure	failure	failure	Success
	30	failure	failure	Success	Success
	20	failure	Success	Success	Success
	10	failure	Success	Success	Success

Table 7. FGSM attacks on the simulated space rendezvous scenario with $\epsilon=0.01$
 $\epsilon = 0.01$

Continuously Attacked Frame	5	10	15	20	
Attack start point (m)	60	failure	failure	failure	failure
	50	failure	failure	failure	failure
	40	failure	failure	failure	failure
	30	failure	failure	failure	failure
	20	failure	failure	failure	failure
	10	failure	failure	failure	failure

From Table 3 - 7, we can clearly see that the adversarial attack can result in a significant impact on the guidance scheme if DNN-based relative navigator is attacked, typically when the distance between the camera and the target is less than 30m. In most cases, continuously attacking the deep model for more than 15 frames after the camera approaches less than 30m to the target, the camera (spacecraft) will fail to reach the target position. In a real space rendezvous mission where a chaser relies on a DL-based relative pose estimation system, an adversarial attack has the potential to cause the chaser to fail in approaching the target position, resulting in mission failure. Therefore, detecting adversarial attacks on DL-based pose estimators becomes critical.

4.1.3. LSTM-based Adversarial Attack Detector

The proposed adversarial attack detector is designed based on the LSTM architecture. It aims to detect the change in SHAP values when an adversarial attack occurs on the input image. As mentioned in Section 3, the SHAP values are computed at the output of the GAP layer in the proposed deep relative pose estimator. The GAP layer contains 1000 neurons, therefore, 1000 values are calculated for each output neuron, resulting 9×1000 output SHAP values.

In our approach, the SHAP values of the GAP layer are calculated by DeepSHAP (Lundberg & Lee, 2017) algorithm. The DeepSHAP algorithm computes SHAP values for inputs by integrating over background samples. It then estimates approximate SHAP values in a manner that sums up the difference between the expected deep model's output on the background samples and the current model's output. In this work, 1000 images are randomly selected from the training dataset to compute the downsampled features at the GAP layer. These samples serve as the background samples for the DeepSHAP explainer. To train the adversarial attack detector, we generated 15,000 sets of SHAP values for normal samples and an additional 15,000 sets of SHAP values for adversarial samples. The normal samples consist of the entire test dataset, which is used for testing the deep pose estimator, along with a random selection of images from the training dataset. This random selection

was made to reach a total of 15,000 samples, thereby bridging the gap between this number and the number of images in the test dataset by the deep relative pose estimator. The adversarial instances are crafted by launching attacks on the DRLs at arbitrary time steps with random ϵ values: 0.5, 0.3, 0.1, 0.05, and 0.01. Subsequently, 3,000 perturbed images are randomly selected from each ϵ value for calculating the corresponding SHAP values.

The SHAP values for both normal and adversarial samples are split into a training and testing set using a 0.8 train-test ratio, resulting in 24,000 samples for training and 6,000 samples for testing. The adversarial attack detector is trained using the Stochastic Gradient Descent (SGD) method with the Adadelta optimiser for 1,000 epochs. After training the adversarial attack detector, it achieved a training accuracy of 99.98% and a test accuracy of 99.90% on the test dataset. In this case, the detection accuracy is calculated by Eq. (9)

$$accuracy = \frac{\text{successful Detection}}{\text{Total No. of Frames}} \times 100\% \quad (9)$$

where the *successful Detection* is defined by that the input frames with the adversarial attack are detector as *True* and frames without adversarial attack are detector as *False*. The experimental results show that the proposed detector can successfully detect adversarial attacks on the DL-based relative pose estimator with high accuracy. The adversarial attack detector is integrated with the deep relative pose estimator and the DeepSHAP explainer to enhance accuracy in space rendezvous scenarios. The overall system is presented in Fig. 8.

The adversarial attack detector is then tested with three trajectories. In each trajectory, the camera (spacecraft) starts 60 meters away from the target, positioned at various points in the x and y directions within the range of $[\pm 25, \pm 15]$. The camera is oriented directly toward the target, with an attitude represented as quaternion (1, 0, 0, 0). The end position is (0, 0, 10). The camera (spacecraft) moves linearly at a rate of 0.25 meters per frame along the z -axis. It follows a projectile trajectory in the x and y directions, resulting in a total of 2,500 frames for each trajectory. The FGSM attack is applied to test trajectories

Table 8. The average accuracy of the adversarial attack detector in test trajectories with various ϵ values.

ϵ	Trajectory	Detection Accuracy
0.5	1	100%
	2	100%
	3	100%
0.3	1	100%
	2	100%
	3	99.98%
0.1	1	99.96%
	2	99.98%
	3	99.96%
0.05	1	100%
	2	99.98%
	3	99.98%
0.01	1	97.06%
	2	96.94%
	3	99.02%
Average		99.21%

with an attack probability of 0.2. Once FGSM is initiated, attacks continue for the subsequent 5 frames. The results of the proposed adversarial attack detector are presented in Table 8. From the test results, the proposed adversarial attack detector successfully detects all incoming FGSM attacks when the $\epsilon = 0.5$. As the ϵ value goes small, i.e. fewer perturbations are made to input images, the detection accuracy has slightly dropped. For these three test trajectories, the proposed adversarial attack detector achieves a detection accuracy of 99.21% on average.

4.2. Experimental Results on Real Data

In previous experiments, both the proposed deep relative pose estimator and the adversarial attack detector exhibited high accuracy on synthetic data. To further evaluate the performance of both systems, we tested them with real-world images obtained from the Autonomous Systems and Machine Intelligence Laboratory (ASMI Lab) at City, University of London. These data include sensor noise, camera calibration noise, ground truth measurement noise, and different lighting conditions that are not present in the training synthetic images.

4.2.1. Accuracy of the Spacecraft Deep Relative Pose Estimator

At the ASMI Lab, a scaled mock-up model of the Jason-1 spacecraft is constructed. This mock-up model is 1/9 the size of the actual Jason-1 spacecraft. The vision sensor ap-

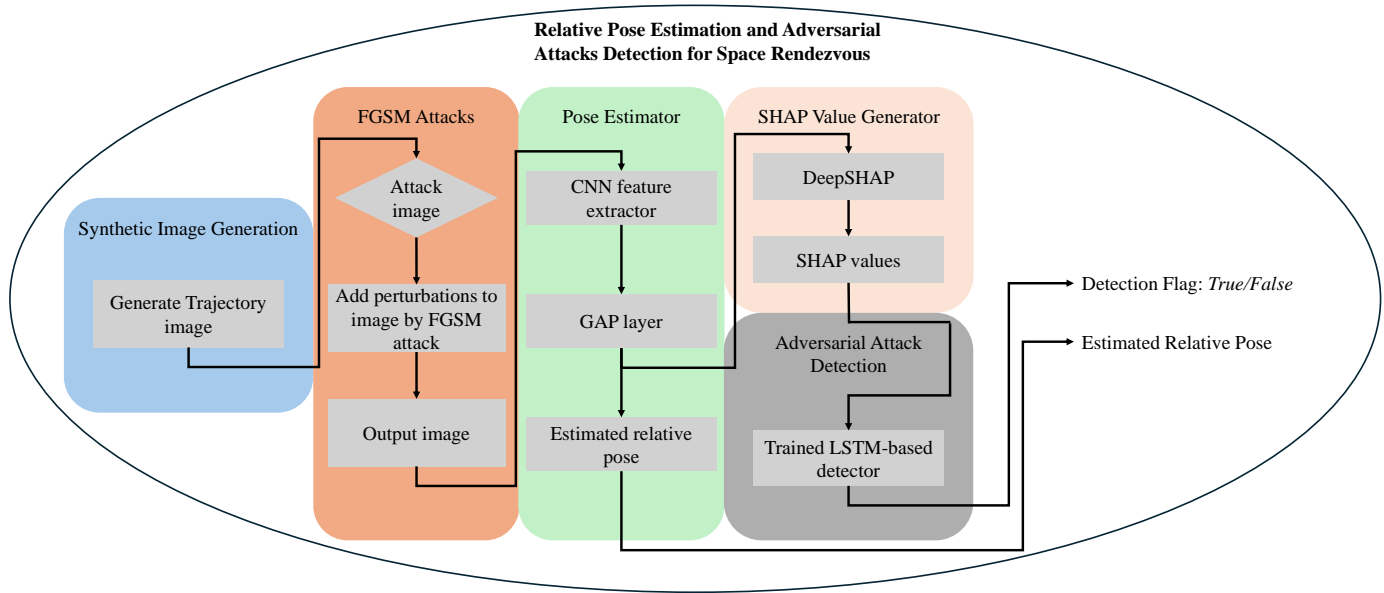


Fig. 8. The experimental system includes the integration of an adversarial attack detector with the relative pose estimator and SHAP values generator.

652 plied for real data acquisition is the ZED 2 camera, which out-
 653 puts images with a resolution of 1920×1080 . The deep relative
 654 pose estimator is retrained on new synthetic data, referred to
 655 as the Synthetic-Lab Dataset, with an input RGB image size of
 656 480×270 to match the aspect ratio of the camera used in the
 657 ASMI Lab. As before, the Synthetic-Lab Dataset is generated
 658 using Blender, where the target was replaced with a 3-D model
 659 of the ASMI Lab mock-up Jason-1. To simulate the space ren-
 660 dezvous scenario over a distance range from 60m to 10m, the
 661 3-D model is scaled up by a factor of 9 in Blender data genera-
 662 tion. An example of the re-training images is shown in Fig. 9

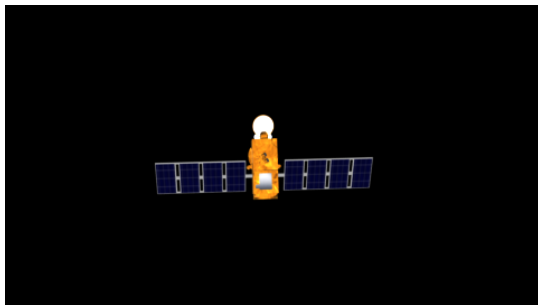


Fig. 9. An example of images generated from Blender for training the pose estimator.

663 Similar to the previous synthetic data experiment, multiple
 664 trajectories are generated to collect images from the Blender,

652 resulting in a total of 32,500 images on Synthetic-Lab Dataset
 653 for training and testing. The hyperparameter settings for train-
 654 ing are the same as the settings applied in previous synthetic
 655 data experiment, including the learning rate, optimiser, batch
 656 size, and data augmentation methods. The pose estimator was
 657 trained for 100 epochs with a train/test split of 0.8.
 658

661 There are three sets of images captured from the ASMI
 662 Lab, referred to as the ASMI Dataset, with each set contain-
 663 ing a total of 750 images. To acquire images for the ASMI
 664 Dataset, the camera movement is controlled by the Rethink
 665 Robotics Sawyer (Sawyer| Rethink Robotics) moving along the
 666 z -axis, and the ground truths relative poses of the images in
 ASMI Dataset are recorded by the OptiTrack Motion Capture
 Systems (OptiTrack). The OptiTrack Motion Capture System
 records the position and attitude of the ASMI Lab mock-up
 Jason-1 and the ZED camera at a frame rate of 120 frames
 per second and assigns a timestamp to each frame. Images are
 acquired by the ZED camera at a resolution of 1920×1080
 and a frame rate of 30 frames per second, with relevant times-
 tamps. The ground truth pose for each frame acquired by the
 ZED camera are assigned by matching the corresponding times-
 tamps from the OptiTrack Motion Capture System. Then, the

relative ground truth position is calculated by the difference between the actual positions of the ZED camera and the ASMI Lab mock-up Jason-1, as shown in Eq. (10),

$$Pos_{lab} = Pos_{camera} - Pos_{target} \quad (10)$$

where Pos_{lab} donates relative ground truth position in ASMI Dataset. The Pos_{camera} and Pos_{target} donate the actual position of the ZED camera and ASMI Lab mock-up Jason-1 recorded by OptiTrack Motion Capture System, respectively.

Due to different camera intrinsic matrices applied between the Synthetic-Lab Dataset and ASMI Dataset, to represent the relative position in the trained model, the position ground truths of the ASMI Dataset are collaborated with the camera view by the following processing:

$$K_{Blender} = \begin{bmatrix} 640 & 0 & 240 \\ 0 & 360 & 135 \\ 0 & 0 & 1 \end{bmatrix} \quad (11)$$

$$K_{zed} = \begin{bmatrix} 1400.41 & 0 & 956.29 \\ 0 & 1400.41 & 557.258 \\ 0 & 0 & 1 \end{bmatrix} \quad (12)$$

$$Target_{real} = 9 \times Target_{lab} \quad (13)$$

$$Pos_{real} = 1400.41 \times \frac{240}{956.29} \times \frac{Target_{lab}}{Target_{real}} \times \frac{1}{640} \times Pos_{lab} \quad (14)$$

where $K_{Blender}$ and K_{zed} represent the camera intrinsic matrices for the camera used in Synthetic-Lab Dataset collection and the ZED camera that is used to acquire images in the ASMI Lab, respectively. $Target_{real}$ and $Target_{lab}$ indicate the target sizes in the Blender 3-D model and the actual size in the ASMI Lab. Pos_{real} and Pos_{lab} denote the relative position of the target in the pose estimator and the ground truth position in the ASMI Lab, respectively. Table 9 illustrates the range of relative positions in the ASMI Dataset and representative relative positions in trained pose estimator. Furthermore, all images in the ASMI Dataset are segmented with a black background and resized to 480×270 to fit the input image size of the trained pose estimator. An example of images captured in ASMI Lab is shown in Fig. 10.

Once the deep relative pose estimation model is trained, it is initially tested on the test set of Synthetic-Lab Dataset, followed then by testing its prediction accuracy on real world data

Table 9. Camera moving range on ASMI Dataset and its representative range on trained pose estimator. The camera is moving along the z -axis. The representative range is calculated by Eq. (14).

trajectory ID	ASMI Lab Range (z-axis)	Representative Range(m)
ASMI-1	3.122 - 2.569	51.180 - 42.11
ASMI-2	2.296 - 1.748	37.64 - 28.66
ASMI-3	1.564 - 1.015	25.64 - 16.64

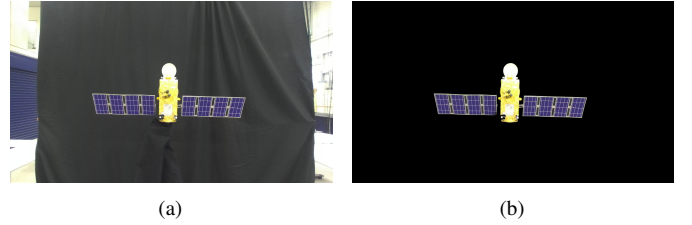


Fig. 10. Examples of images captured in ASMI Dataset. (a) Original image captured in ASMI Lab (b) Segmented image with black background.

captured from the ASMI Lab, i.e. ASMI Dataset. The prediction accuracy of the deep relative pose estimator is reported in Fig. 11. Similar to the previous synthetic testing, position error and attitude error are calculated by Eq. (5) and Eq. (6), respectively. Compared with the prediction accuracy on the Synthetic-Lab Dataset, the position error of the ASMI Dataset is slightly higher. This could be attributed to variations in the illumination conditions compared to the Synthetic-Lab Dataset, as well as factors such as ground truth measurement noise and camera calibration noise. On the other hand, the predicted attitude error in the ASMI Dataset is much smaller than the synthetic data. One possible reason could be that the target remains stable at a fixed position with rotation effects during the images capture.

4.2.2. FGSM Attacks on ASMI Dataset

To evaluate how the pose estimator can be impacted by adversarial attacks on real data, the FGSM attack is then applied to the ASMI Dataset. In this case, the FGSM is configured as the same ϵ as previously applied in synthetic, including 1, 0.5, 0.3, 0.1, 0.05 and 0.01. In this experiment, all images are perturbed by the FGSM attack. The model's average prediction error under FGSM attacks with various ϵ values on the ASMI Dataset are illustrated in Fig. 12.

As shown in Fig. 12, FGSM has a significant impact on position estimation but only slight impacts on attitude estimation. In comparison to the previous experiment with synthetic data,

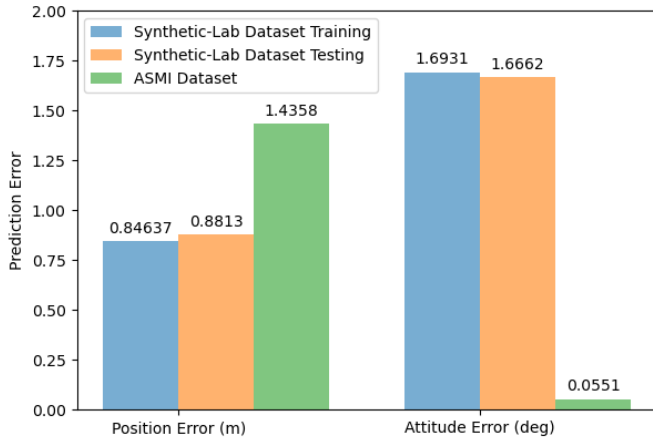


Fig. 11. The prediction accuracy of the proposed pose estimator on Synthetic-Lab Dataset and ASMI Dataset after 100 epochs. The blue bar presents the average error on training data and the orange bar represents the average error on test data on Synthetic-Lab Dataset. The green bar indicates the average error on the ASMI Dataset.

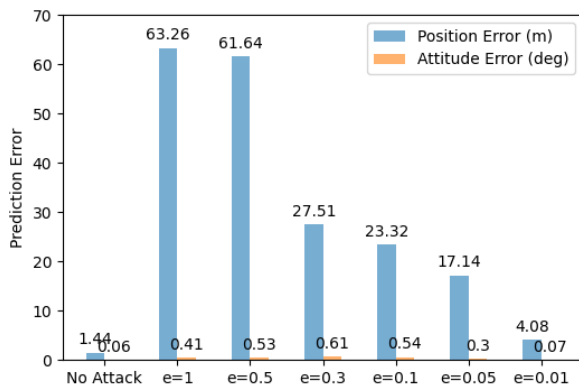


Fig. 12. Comparison of the prediction error under FGSM attack on ASMI Dataset with various ϵ values. The blue bar indicates the average position error in meter and the orange bar represents the average attitude error in degrees.

the FGSM attack has a more pronounced effect when ϵ is less than 0.05 on the predicted position in the ASMI Dataset. However, the attitude error remains quite stable, typically less than 1 degree, for all tested ϵ values.

4.2.3. LSTM-based Adversarial Attack Detector

To evaluate the adversarial attack detector on the ASMI Dataset, SHAP values are obtained by processing the pose estimator on the Synthetic-Lab Dataset. Similar to the previous synthetic data experiment, the SHAP values are obtained from the output of the GAP layer in the deep relative pose estima-

tor by DeepSHAP algorithm. 1,000 images from the training data on Synthetic-Lab Dataset are randomly selected to generate background data. A total of 30,000 SHAP value samples, consisting of 15,000 normal samples and 15,000 adversarial samples, are used to train the adversarial attack detector. The 15,000 normal samples consist of all images from the test data on the Synthetic-Lab Dataset and randomly selected images from the training data to account for the difference between 15,000 and the total number of images in the test data. Adversarial samples are generated by applying FGSM attacks to the normal sample images with randomly selected ϵ values from [0.5, 0.3, 0.1, 0.05, 0.01].

The SHAP values are shuffled and split by a train-test ratio of 0.8, i.e. 24,000 samples for training and 6,000 samples for testing. The adversarial attack detector is trained by SGD with an Adadelta optimiser for 2000 epochs. Early termination is implemented to reduce the training time. To do that, the training data are further split into 80% for training and 20% for validation. If the validation loss does not decrease over 20 epochs, the training process will be terminated. After the early termination condition, the proposed adversarial attack detector achieves a detection accuracy of 99.18% on training data and 98.8% on test data.

Subsequently, the pose estimator, FGSM attacks, and adversarial attack detector are integrated to evaluate the overall performance on the ASMI Dataset. The integrated system is identical to the one shown in Fig. 8, with the exception that the 'Blender Image Generation' part is replaced by the ASMI Dataset. In the ASMI Dataset, a random attack probability of 0.2 is applied to FGSM attacks. When an attack occurs, input images are continuously perturbed by FGSM for the next 10 frames. The detection accuracy is calculated by Eq. (9). Table 10 presents the detection accuracy on the ASMI Dataset for various ϵ values.

As shown in Table 10, the proposed adversarial attack detector achieves an average correct detection rate of 96.29% on the ASMI Dataset. The accuracy slightly drops when the ϵ value becomes smaller, which is caused by fewer perturbations ap-

Table 10. The average accuracy of the adversarial attack detector in ASMI Dataset with various ϵ values.

ϵ	Detection Accuracy
0.5	100 %
0.3	100 %
0.1	100 %
0.05	98.44%
0.01	90.44 %
Average	96.29 %

plied to the input images as ϵ decreases.

5. Conclusion

This paper firstly examines the impact of adversarial attacks on DL-based spacecraft relative pose estimation in space rendezvous scenarios. To do this, a CNN-based relative pose estimation algorithm is proposed. FGSM adversarial attacks are implemented, which have a significant impact on the model's predictions. Subsequently, an LSTM-based adversarial attack detector is proposed to identify adversarial attacks on input images. XAI techniques are adopted to analyse the model's predictions and generate SHAP values-based explanations for the model's predictions. Multiple experiments are carried out to evaluate the performance of the CNN-based spacecraft relative pose estimator, how the adversarial attacks can impact on DL-based pose estimator in space rendezvous missions, and the performance of the proposed adversarial attack detector. The proposed methods have been tested on both synthetic and real image datasets. The results show that the adversarial attack detector performs robustly in detecting adversarial attacks, achieving an average of 99.21% detection rate on synthetic data and 96.29% on real data collected from the ASMI Lab.

Although the impact of digital adversarial attacks on DL-based spacecraft relative pose estimation has been analysed in this work, how to physically implement the adversarial attacks still needs to be explored. Moreover, the proposed method demonstrates high accuracy in detecting adversarial attacks for the DL-based spacecraft relative pose estimation, how to correct the estimated pose after detecting adversarial attacks becomes critical to provide a robust DL-based system for future space missions.

Acknowledgments

This work is funded by the European Space Agency (ESA),
Project ID: ESA AO/2-1856/22/NL/GLC/ov.

References

- Cebollada, S., Payá, L., Jiang, X. et al. (2022). Development and use of a convolutional neural network for hierarchical appearance-based localization. *Artificial Intelligence Review*, (pp. 1–28).
- Chawla, H., Varma, A., Arani, E. et al. (2022). Adversarial attacks on monocular pose estimation. In *2022 IEEE/RSJ International Conference on Intelligent Robots and Systems (IROS)* (pp. 12500–12505). IEEE.
- Chekakta, Z., Zenati, A., Aouf, N. et al. (2022). Robust deep learning lidar-based pose estimation for autonomous space landers. *Acta Astronautica*, 201, 59–74.
- Deng, J., Dong, W., Socher, R. et al. (2009). Imagenet: A large-scale hierarchical image database. In *2009 IEEE conference on computer vision and pattern recognition* (pp. 248–255). Ieee.
- Goodfellow, I. J., Shlens, J., & Szegedy, C. (2014). Explaining and harnessing adversarial examples. *arXiv preprint arXiv:1412.6572*, .
- Grabinski, J., Keuper, J., & Keuper, M. (2022). Aliasing and adversarial robust generalization of cnns. *Machine Learning*, 111(11), 3925–3951.
- Guo, Y., Liu, Y., Oerlemans, A. et al. (2016). Deep learning for visual understanding: A review. *Neurocomputing*, 187, 27–48.
- He, K., Zhang, X., Ren, S. et al. (2016). Deep residual learning for image recognition. In *Proceedings of the IEEE conference on computer vision and pattern recognition* (pp. 770–778).
- Hickling, T., Aouf, N., & Spencer, P. (2023). Robust adversarial attacks detection based on explainable deep reinforcement learning for uav guidance and planning. *IEEE Transactions on Intelligent Vehicles*, .
- Ilahi, I., Usama, M., Qadir, J. et al. (2021). Challenges and countermeasures for adversarial attacks on deep reinforcement learning. *IEEE Transactions on Artificial Intelligence*, 3(2), 90–109.
- Ioffe, S., & Szegedy, C. (2015). Batch normalization: Accelerating deep network training by reducing internal covariate shift. In *International conference on machine learning* (pp. 448–456). pmlr.
- Jason-1 3D Model (Accessed on 16 October 2023 <http://nasa3d.arc.nasa.gov/detail/jason-1>).
- Kelvins - ESA's Advanced Concepts Competition Website (Accessed October, 2023. <https://kelvins.esa.int/satellite-pose-estimation-challenge/data/>).
- Kendall, A., Gal, Y., & Cipolla, R. (2018). Multi-task learning using uncertainty to weigh losses for scene geometry and semantics. In *Proceedings of the IEEE conference on computer vision and pattern recognition* (pp. 7482–7491).
- Kisantal, M., Sharma, S., Park, T. H. et al. (2020). Satellite pose estimation challenge: Dataset, competition design, and results. *IEEE Transactions on Aerospace and Electronic Systems*, 56(5), 4083–4098.
- Krizhevsky, A., Sutskever, I., & Hinton, G. E. (2012). Imagenet classification with deep convolutional neural networks. *Advances in neural information processing systems*, 25.
- Lin, Y., Zhao, H., Ma, X. et al. (2020). Adversarial attacks in modulation recognition with convolutional neural networks. *IEEE Transactions on Reliability*, 70(1), 389–401.
- Liu, H., Zhang, D., & Chen, H. (2020). Towards robust classification detection for adversarial examples. In *2020 15th International Conference for Internet Technology and Secured Transactions (ICITST)* (pp. 1–7). IEEE.
- Liu, L., Wang, L., & Liu, X. (2011). In defense of soft-assignment coding. In *2011 International Conference on Computer Vision* (pp. 2486–2493). IEEE.
- Lundberg, S. M., & Lee, S.-I. (2017). A unified approach to interpreting model predictions. *Advances in neural information processing systems*, 30.
- Nazari, M., Kluge, A., Apostolova, I. et al. (2022). Explainable ai to improve acceptance of convolutional neural networks for automatic classification of dopamine transporter spect in the diagnosis of clinically uncertain parkinsonian syndromes. *European journal of nuclear medicine and molecular imaging*, (pp. 1–11).

- 886 Nemcovsky, Y., Jacoby, M., Bronstein, A. M. et al. (2022). Physical passive
887 patch adversarial attacks on visual odometry systems. In *Proceedings of the*
888 *Asian Conference on Computer Vision* (pp. 1795–1811).
- 889 Oestreich, C., Lim, T. W., & Broussard, R. (2020). On-orbit relative pose ini-
890 tialization via convolutional neural networks. In *AIAA Scitech 2020 Forum*
891 (p. 0457).
- 892 OptiTrack (Accessed October, 2023. <https://www.optitrack.com/>).
- 893 Persson, S., Bodin, P., Gill, E. et al. (2006). Prisma-an autonomous formation
894 flying mission, .
- 895 Phisannupawong, T., Kamsing, P., Torteeka, P. et al. (2020). Vision-based
896 spacecraft pose estimation via a deep convolutional neural network for non-
897 cooperative docking operations. *Aerospace*, 7(9), 126.
- 898 Pope, P. E., Kolouri, S., Rostami, M. et al. (2019). Explainability methods
899 for graph convolutional neural networks. In *Proceedings of the IEEE/CVF*
900 *conference on computer vision and pattern recognition* (pp. 10772–10781).
- 901 Proença, P. F., & Gao, Y. (2020). Deep learning for spacecraft pose estimation
902 from photorealistic rendering. In *2020 IEEE International Conference on*
903 *Robotics and Automation (ICRA)* (pp. 6007–6013). IEEE.
- 904 Redmon, J., & Farhadi, A. (2017). Yolo9000: better, faster, stronger. In *Pro-*
905 *ceedings of the IEEE conference on computer vision and pattern recognition*
906 (pp. 7263–7271).
- 907 Redmon, J., & Farhadi, A. (2018). Yolov3: An incremental improvement. *arXiv*
908 *preprint arXiv:1804.02767*, .
- 909 Ren, S., He, K., Girshick, R. et al. (2017). Faster r-cnn: Towards real-time ob-
910 ject detection with region proposal networks. *IEEE transactions on pattern*
911 *analysis and machine intelligence*, 39(6), 1137.
- 912 Rondao, D., Aouf, N., & Richardson, M. A. (2022). Chinet: Deep recurrent
913 convolutional learning for multimodal spacecraft pose estimation. *IEEE*
914 *Transactions on Aerospace and Electronic Systems*, .
- 915 Sawyer| Rethink Robotics (Accessed October, 2023. [https://www.](https://www.rethinkrobotics.com/sawyer)
916 [rethinkrobotics.com/sawyer](https://www.rethinkrobotics.com/sawyer)).
- 917 Selvaraju, R. R., Cogswell, M., Das, A. et al. (2017). Grad-cam: Visual expla-
918 nations from deep networks via gradient-based localization. In *Proceedings*
919 *of the IEEE international conference on computer vision* (pp. 618–626).
- 920 Sharma, S., Beierle, C., & D’Amico, S. (2018). Pose estimation for non-
921 cooperative spacecraft rendezvous using convolutional neural networks. In
922 *2018 IEEE Aerospace Conference* (pp. 1–12). IEEE.
- 923 Shrikumar, A., Greenside, P., & Kundaje, A. (2017). Learning important fea-
924 tures through propagating activation differences. In *International conference*
925 *on machine learning* (pp. 3145–3153). PMLR.
- 926 Simonyan, K., Vedaldi, A., & Zisserman, A. (2013). Deep inside convolutional
927 networks: Visualising image classification models and saliency maps. *arXiv*
928 *preprint arXiv:1312.6034*, .
- 929 Smith, L. N. (2017). Cyclical learning rates for training neural networks. In
930 *2017 IEEE winter conference on applications of computer vision (WACV)*
931 (pp. 464–472). IEEE.
- 932 Song, J., Rondao, D., & Aouf, N. (2022). Deep learning-based spacecraft rela-
933 tive navigation methods: A survey. *Acta Astronautica*, 191, 22–40.
- 934 Tian, J., Shen, C., Wang, B. et al. (2024). Lesson: Multi-label adversarial false
935 data injection attack for deep learning locational detection. *IEEE Transac-*
936 *tions on Dependable and Secure Computing*, .
- 937 Wang, C., & Aouf, N. (2024). Explainable deep adversarial reinforcement
938 learning approach for robust autonomous driving. *IEEE Transactions on*
939 *Intelligent Vehicles*, .
- 940 Wie, B., Lappas, V., & Gil-Fernández, J. (2014). Attitude and orbit control
941 systems. *The International Handbook of Space Technology*, (pp. 323–369).
- 942 Yang, X., Song, J., She, H. et al. (2021). Pose estimation of non-cooperative
943 spacecraft based on convolutional neural network. In *2021 40th Chinese*
944 *Control Conference (CCC)* (pp. 8433–8438). IEEE.
- 945 Yu, Y., Si, X., Hu, C. et al. (2019). A review of recurrent neural networks: Lstm
946 cells and network architectures. *Neural computation*, 31(7), 1235–1270.
- 947 Zhou, B., Khosla, A., Lapedriza, A. et al. (2016). Learning deep features for
948 discriminative localization. In *Proceedings of the IEEE conference on com-*
949 *puter vision and pattern recognition* (pp. 2921–2929).
- 950 Zhou, Y., Barnes, C., Lu, J. et al. (2019). On the continuity of rotation repre-
951 sentations in neural networks. In *Proceedings of the IEEE/CVF Conference*
952 *on Computer Vision and Pattern Recognition* (pp. 5745–5753).